Journal Of Geophysical Research
MAY 11 2007; 112 (C5) NIL_80-NIL_97
http://dx.doi.org/10.1029/2006JC003878

Archimer http://www.ifremer.fr/docelec/
Archive Institutionnelle de l'Ifremer

An edited version of this paper was published by AGU.

Microcanonical multifractal formalism: application to the estimation of ocean surface velocities

J. Isern-Fontanet[1,2,], A. Turiel[2,], E. García-Ladona[2,], J. Font[2,]

[1] Departement d'Océanographie Physique et Spatiale, IFREMER Centre de Brest, Technôpole de Brest-Iroise, Plouzané, France
[2] Institut de Ciències del Mar (CSIC), Barcelona, Spain

Abstract:

In this paper we investigate the validity of the multifractal formalism to study sea surface temperature (SST). It is shown that SST patterns observed in moderate resolution SST images have anomalous scaling properties characteristic of a multifractal structure. The most probable origin of the observed structures is the turbulent character of the oceanic flow as they evolve slowly and are very persistent in times compatible with ocean mesoscale dynamics (several days). The spectrum of singularity exponents indicates that the dynamics of the processes leading to the geometrical arrangement of the SST patterns is quite general over the available range of scales. As a consequence, multifractal techniques can be used to extract properties of the underlying flow. In particular, the geometry of the SST multifractal components is closely linked with the ocean flow, which allows to build a reasonable guess of the streamfunction (defined as the maximum singular streamfunction (MSS)) from a single SST image. Thus the ocean surface velocity field can be easily inferred, with some limitations. As multifractal analysis is in essence a geometrical approach, the method is able to retrieve a high resolution velocity field, well localized in space, but with some indetermination on the modulus and sense of velocity vectors. To solve this, a general framework for the integration of extra information is proposed, what is illustrated with an example merging MSS with altimetric data.

Keywords: MSS method; remote sensing; operational oceanography

Microcanonical multifractal formalism: application to the estimation of ocean surface velocities

J. Isern-Fontanet, A. Turiel, E. García-Ladona, J. Font

Institut de Ciències del Mar (CSIC), Barcelona, Spain

Abstract. In this paper we investigate the validity of the multifractal formalism to study Sea Surface Temperature (SST). It is shown that SST patterns observed in moderate resolution SST images have anomalous scaling properties characteristic of a multifractal structure. The most probable origin of the observed structures is the turbulent character of the oceanic flow as they evolve slowly and are very persistent in times compatible with ocean mesoscale dynamics (several days). The spectrum of singularity exponents indicates that the dynamics of the processes leading to the geometrical arrangement of the SST patterns is quite general over the available range of scales. As a consequence, multifractal techniques can be used to extract properties of the underlying flow. In particular, the geometry of the SST multifractal components is closely linked with the ocean flow, which allows to build a reasonable guess of the sreamfunction (defined as the Maximum Singular sreamfunction, MSS) from a single SST image. Thus, the ocean surface velocity field can be easily inferred, with some limitations. As multifractal analysis is in essence a geometrical approach, the method is able to retrieve a high resolution velocity field, well localised in space, but with some indetermination on the modulus and sense of velocity vectors. To solve this, a general framework for the integration of extra information is proposed, what is illustrated with an example merging MSS with altimetric data.

1. Introduction

In spite of the great importance of understanding turbulent dynamics to provide an adequate picture of many geophysical processes, turbulence is still one of the major unsolved problems in fluid dynamics. Due to their chaotic shape, turbulent flows cannot be easily described with some few global quantities, and hence an enormous amount of degrees of freedom must be retained to properly describe them. From all approaches to turbulence, the most successful one is the statistical analysis, favoured by the existence of many independent degrees of freedom at all scales contributing to the final motion. However, turbulence gives rise to intermittency and so the distributions of the relevant quantities have heavy tails; as a consequence, statistical analyses of turbulent flows demand a great amount of data to obtain reliable estimates of dynamical quantities. This has also been the case in geophysical flows, where reliable statistical analysis have been mostly restricted to small scale flows. We know much more properties about geostrophic turbulence from numerical modeling than from the direct analysis of observations.

Earth observation satellites has been a great revolution allowing for the first time ocean processes to be adequately sampled [*Munk*, 2000]. Remote sensing have uncovered a picture of the ocean characterized by a complex geometry, crowded with eddies of different sizes and filamentary structures similar to what theory predicts. The range of scales covered by infrared or colour images span over three decades (roughly from one to thousand of kilometers) and they are acquired several times per day. Consequently, remote sensing data sets are today in a stage to furnish the best framework, in which techniques and concepts developed for the study of turbulent flows may lead to better understand the statistical properties of the complex ocean dynamics. Some examples of this approach are the characterization of ocean vortices [e.g. *Isern-Fontanet et al.*, 2003; *Morrow et al.*, 2004; *Isern-Fontanet et al.*, 2006b], velocity statistics [*Llewellyn Smith and Gille*, 1998; *Gille and Smith*, 2000; *Isern-Fontanet et al.*, 2006c] or the stirring properties of the ocean [e.g. *Abraham and Bowen*, 2002; *Waugh et al.*, 2006].

Many of such studies rely on the knowledge of the ocean velocity field which is difficult to be directly measured from remote sensing. Despite very recent advances in space borne radar technology [e.g. *Chapron et al.*, 2005], presently surface ocean horizontal velocities are regularly estimated from altimetric measurements. However, altimeters only provide information about the cross-track geostrophic velocity. Then, interpolation methods are required to recover both components of surface velocities [e.g. *Le Traon and Ogor*, 1998], which has the effect of strongly reduced the capability to investigate wavelengths below 100 km [e.g. *Ducet et al.*, 2000]. Alternatively, many efforts have been previously done to estimate surface currents from infra-red sensors through different methodologies [i.e. *Emery et al.*, 1986; *Kelly*, 1989; *Whal and Simpson*, 1991; *Wu et al.*, 1992; *Vigan et al.*, 2000a, b; *Bowen et al.*, 2002]. A general characteristic of the existing methods is the requirements of having a cloud-free time-series of images.

Recently, a different approach has been introduced based on the geometrical properties of advected tracers [*Turiel et al.*, 2005b]. Coherent vortices in a turbulent flow strongly interact, which has the effect of permanently stretch and fold small-scale filaments ejected from vortex cores and generate small-scale tracer gradients between eddies. Therefore, the spatial structure of a tracer inherits some properties of the underlying flow, in according to what has been theoretically and experimentally shown in some works [*Abraham and Bowen*, 2002; *Turiel et al.*, 2005b, a]. This has the effect of organizing the geometry of the flow as a hierarchy of fractal sets, called singularity manifolds, each one associated to a singularity exponent: this is the so-called multifractal

0148-0227/06/$9.00

formalism for fully developed turbulence (FDT) [*Parisi and Frisch*, 1985; *Frisch*, 1995]. This geometrical arrangement of the flow is intimately linked to the energy cascade, which allows to study its properties from the geometrical properties of any tracer for which advection is important enough. Furthermore, as singularity manifolds are advected by the flow, assessing tracer singularities allows to detect the main streamlines, and then, through a suitable interpolation algorithm, the sreamfunction of the flow could be reconstructed [*Turiel et al.*, 2005b, a].

A key point in this approach is the assumption of a multifractal structure on tracer images. In the context of atmospheric flows, there are many evidences of such a multifractal hierarchy [i.e. *Chigirinskaya et al.*, 1994; *Lovejoy et al.*, 2001; *Sachs et al.*, 2002; *Turiel et al.*, 2005a]. In the ocean, time series of temperature, fluorescence and other biochemical tracers also exhibit multifractal characteristics [*Lovejoy et al.*, 2001]. However, up to our knowledge there are no evidence on the multifractal properties of the geometrical arrangement of ocean tracers, as for instance the spatial distribution of SST. If this is verified and assuming that the dynamics of the ocean is similar to that corresponding to FDT, one can reasonably expect that tracers in the ocean possess the same singularity manifolds as the underlying turbulent ocean flows. Thus we should be able to deal with a method to estimation of the velocity field of the ocean. Therefore, the objective of this paper is twofold. First, it will be shown that moderate resolution SST images of the ocean (Pathfinder SST in our case) exhibit a multifractal structure and, therefore, multifractal techniques as the proposed MSS method can be used to give an estimation of the sreamfunction. Second, the paper discusses the limitations of these multifractal methods and show how the combination with other data (altimetry in this study) can be used to overcome them.

Due to the important and non trivial theoretical concepts which need to be introduced and which deserve full discussion in an oceanographic context, we have decided to organize the text in a progressive way. First, in section 2 we outline the theoretical background of the multifractal formalism, which is the root of the proposed method for the estimation of ocean velocities. Section 3 briefly presents all the data used. Then, in section 4 the method for the estimation of singularities is presented and the validity of the Microcanonical Multifractal Formalism for SST images is verified. After that, the method to retrieve the Maximum Singularity sreamfunction (MSS) and its application to data is presented in section 5. The possible ways to integrate additional information in the framework of MSS are presented in Section 6; we present there the example of integrating altimetry. Finally, an overall discussion and conclusions of the paper are given in section 7.

2. General theory

There exists an extensive scientific literature on the roots of the multifractal formalism in the context of FDT, its connections with anomalous scaling in the structure functions and the geometrical interpretation of scaling exponents in terms of a hierarchy of fractal manifolds [*Parisi and Frisch*, 1985; *Novikov*, 1994; *She and Leveque*, 1994; *Arneodo et al.*, 1995; *She and Waymire*, 1995]. However, there is much less literature establishing the explicit passage from the classical, statistical formalism (based on structure functions and the assessment of the multiplicative cascade), known as Canonical formalism, to the geometrical one (in which Parisi and Frisch's singularity manifolds are explicitly separated from a given signal).

The idea about a geometrical approach to the study of the FDT and microcanonical exponents can be tracked back in the early works by Meneveau, Sreenivasan and collaborators *Chhabra et al.* [1989]; *Meneveau and Sreenivasan* [1991]; *Sreenivasan* [1991] . However, technical limitations on the determination of the local singularity exponents and the greater amount of statistical measurements had left this idea a bit aside. Since then, some progresses have been made in order to uncover geometry from data, mainly concentrated on the extraction of the multiscale skeleton of wavelet transform maxima [*Muzy et al.*, 1991; *Bacry et al.*, 1993; *Arrault et al.*, 1997; *Amaral et al.*, 1998; *Ivanov et al.*, 1999; *Struzik*, 2000]. However, this multiscale skeleton can hardly be used to assign a singularity to each point. In spite of these initial limitations, recent advances in signal processing [*Turiel et al.*, 1998; *Turiel and Parga*, 2000] have allowed to recover the geometrical perspective of the energy cascade allowing to define a new formalism, called the Microcanonical Multifractal Formalism.

2.1. Canonical Formalism

Since the famous Kolmogorov's 1941 papers [*Kolmogorov*, 1941a, b; *Hunt et al.*, 1991], much research has been conducted to explain the properties of fully developed turbulence in terms of scale invariant quantities characterizing the behaviour of statistical averages of some dynamical quantities. In a rather general formulation, we can define the local structure function of order p and size scope r, denoted by $S_p(r)$, as the order-p moment of a dynamical variable ϵ_r, namely:

$$S_p(r) \;=\; \langle \epsilon_r^p \rangle \tag{1}$$

where the average is taken over an appropriate ensemble of realizations or over a single realization large enough when ergodicity or at least stationarity of the moments can be assumed [*Davis et al.*, 1994; *Frisch*, 1995]. The variable ϵ_r must refer to a statistical stationary quantity defined over a given resolution scale r; common choices include linear increments of the velocity,

$$\epsilon_r(\vec{x}) \;=\; |v(\vec{x}) - v(\vec{x}+\vec{r})| \tag{2}$$

and local energy dissipations on balls of radius r,

$$\epsilon_r(\vec{x}) \;=\; \sum_{ij} \int_{B_r(\vec{x})} d\vec{x}' \; \left(\partial_i v_j(\vec{x}') \;+\; \partial_j v_i(\vec{x}')\right)^2 \tag{3}$$

Kolmogorov's 1941 theory predicts that, at any order p, the structure function $S_p(r)$ is scale-invariant with respect to the scale scope r, what manifests in a power-law dependence in the inertial range,

$$S_p(r) \;\propto\; r^{\tau_p} \quad ; \quad r \ll 1 \tag{4}$$

In addition, Kolmogorov predicted that all the multiscaling exponents τ_p could be related in a simple way: they should fit a linear relation,

$$\tau_p \;=\; H\,p \;+\; \beta \tag{5}$$

where the coefficient H is given by the scaling properties of the maximum of ϵ_r,

$$\max_{\vec{x}} \; \epsilon_r(\vec{x}) \;\propto\; r^H \quad ; \quad r \ll 1 \tag{6}$$

while the coefficient β is related to the behaviour of the support of ϵ_r (*i.e.*, the set where ϵ_r is different from zero), in the way:

$$r^{\beta} \propto S_0(r) = \int d\vec{x}' \; 1_{\epsilon_r(\vec{x}')\neq 0} \tag{7}$$

According to Kolmogorov's model of linear multiscaling exponents, the energy is concentrated on a fractal manifold, given by the support, at which all the points contribute exactly the same, namely r^H. We can immediately deduce the dimension of this fractal manifold by the scaling property given by equation (7); following Falconer [*Falconer*, 1990], the support scales as r^{d-D}, where d is the dimension of the embedding space ($d = 2$ in the case of 2D turbulence) and D is the fractal dimension of the support. Hence, comparing with equation (7) we have $D = d - \beta$.

It was soon realized that the linear scaling proposed by Kolmogorov did not fit experimental curves; experimental τ_p [*Arneodo et al.*, 1996] present "anomalous scaling", that is, a marked separation from the linear behaviour. The curvature of τ_p makes Kolmogorov's picture a bit more complex. Now, the points in the support do not possess the same scaling r^H any more; instead, the support is split in different scaling fractal components (manifolds), each one scaling differently. We are hence constrained to pass from a single fractal scheme to a multiple fractal framework.

A simple empirical obtention of the multiscaling exponents τ_p is not enough to provide a theoretical insight on the process which give rise to the scale-invariant properties of fully developed turbulence. It was then required to introduce a model to explain anomalous scaling: the multiplicative cascade. First, for any $0 < \kappa < 1$ let us construct a random variable η_κ such that

$$\langle \eta_\kappa^p \rangle = \kappa^{\tau_p} \tag{8}$$

The existence of such a variable will depend on the properties of τ_p. A necessary condition is the constant concavity/convexity of τ_p as a function of p [*Carleman*, 1922], which is granted because the τ_p are obtained from actual order p-moments. In fact, the concavity of τ_p indicates the sign of the cascading process [*Gupta and Waymire*, 1990] that we will introduce in the following. To simplify the discussion, we will assume that for the variable ϵ_r the cascade is verified as a down-scaling process; the up-scaling counterpart can be easily generalized from this case.

Provided η_κ exists for any κ and recalling the definition of the structure functions, equation (1), for any two scales $r < L$ it follows:

$$\langle \epsilon_r^p \rangle = \langle \eta_{\frac{r}{L}}^p \rangle \, \langle \epsilon_L^p \rangle \tag{9}$$

for all p. As a consequence, we can write:

$$\epsilon_r \doteq \eta_{\frac{r}{L}} \, \epsilon_L \tag{10}$$

where the symbol $\doteq$ means that both sides have the same distribution. In equation (10), which is known as the *cascade relation*, it is assumed that $\eta_{\frac{r}{L}}$ is a random variable independent from ϵ_L. The reason for calling such a relation a "cascade" comes from the fact that, if we introduce any intermediate scale r', $r < r' < L$, we obtain:

$$\eta_{\frac{r}{L}} \doteq \eta_{\frac{r}{r'}} \eta_{\frac{r'}{L}} \tag{11}$$

what is trivially verified according to the definition of the cascade variable, equation (8). So that, the cascading process can be verified in any number of intermediate stages and in all cases the final result will be the same: in some sense, the down-scaling injection process is in statistical equilibrium. Equation (11) also implies that the random variables η_κ possess infinitely divisible distributions [*Novikov*, 1994; *She and Waymire*, 1995], what enormously restricts the class of allowed processes. Many experimental facts have confirmed the existence of the cascade in flows under fully developed turbulence [*Chhabra et al.*, 1989; *Frisch*, 1995; *Arneodo et al.*, 1996; *Lovejoy et al.*, 2001]; hints also exist on their presence in oceanic flows [*Abraham and Bowen*, 2002; *Turiel et al.*, 2005b].

The cascading process is a sign of the existence of a tightly hierarchized structure in the flow; however, in the form discussed above, it is just a statistical signature, difficult to relate to definite objects with physical meaning. The first step to establish a link with the geometrical arrangement of flows can probably be traced in Parisi and Frisch's derivation on the multifractal structure of flows under cascading processes [*Parisi and Frisch*, 1985]. They assumed that, due to the anomalous scaling, the points in the support of ϵ_r do not share a single value of scaling exponent H as in Kolmogorov's theory, equation (5). On the contrary, the support is split in different fractal components $\mathcal{F}_h$, each one having a different scaling exponent h. As the fractal manifolds can have different fractal dimensions, we introduce the concept of *singularity spectrum* $D(h)$, defined as the (Hausdorff) fractal dimension of the component $\mathcal{F}_h$. As before, at a scale r the amount of points assigned to a the component $\mathcal{F}_h$ goes as $r^{d-D(h)}$, so the distribution of scaling exponents at a given scale r is given by:

$$\rho_r(h) \propto r^{d-D(h)} \tag{12}$$

According to Parisi and Frisch, the multiscaling exponents τ_p can be immediately related to the singularity spectrum, in the way:

$$\tau_p = \inf_h \{ph + d - D(h)\} \tag{13}$$

Equation (13) is a cornerstone in the multifractal derivation, because it allows relating a geometrical characteristic (the singularity spectrum) with the multiplicative cascade. So that, when we arrive to obtain the singularity exponents in a given realization, we can recover all the properties of the multiplicative cascade. An important feature for the singularity spectrum is to be a convex function of h; under such a circumstance, the Legendre transform in equation (13) can be inverted and the singularity spectrum is calculated from the multiscaling exponents; namely:

$$D(h) = \inf_p \{ph + d - \tau_p\} \tag{14}$$

A well-behaved singularity spectrum should correspond to a convex curve which is one of the requirements in the Microcanonical Multifractal Formalism presented in the following.

2.2. Microcanonical Formalism

To give the final step from statistics to geometry, two additional ingredients are in order. First, we need a method capable to assess the local scaling exponent to be assigned to each point. It should be realized that the concept of local scaling exponent is in fact more easily recognised as the one of Hölder or singularity exponent. The introduction of

singularity exponents allows a generalization of the classical Taylor expansion of functions; in addition, it serves to relate scaling properties of a variable with its regularity properties according to Functional Analysis. Then, the local singularity exponent $h(\vec{x})$ of a given field $s(\vec{x})$ at the point $\vec{x}$ can be obtained, for any vector $\vec{r}$ small enough, from the following scaling

$$\frac{1}{r}|s(\vec{x}+\vec{r}) - s(\vec{x})| \sim r^{h(\vec{x})} \quad (15)$$

Results on wind tunnels and other laboratory experiences reveal that such scalings are generally observed (see *Arneodo et al.* [1996] and cites therein). By means of equation (15), a local singularity exponent $h(\vec{x})$ can be associated to each point $\vec{x}$, which accounts for the local properties of changes in scale of the function s. The singularity exponent informs about the local regularities of the function and its degree of continuity or discontinuity around the given point. The name "singularity exponent" does not necessarily imply that the function is divergent at the point; large values of $h(\vec{x})$, on the contrary, indicate that the function is very smooth [*Arneodo et al.*, 1995]. Expressions as equation (15) are generically known as Singularity Analysis for the function $s(\vec{x})$.

The second ingredient is the relation between the scaling properties of the flow, in general difficult to quantify, to the scaling properties of related variables much more accessible and easily to observe. A typical case is that of scalar variables: quantities on which the flow, as a first approximation, acts as if they were tracers. For purely passive scalars, it immediately follows that the scaling properties appearing in the asymptotic regime are those derived from the scaling on the flow [*Frisch*, 1995]. For non-passive scalars, the ability to relate local scaling exponents emerging from the scalar to those of the flow rely on the assumption than the corrections to the material derivative do not affect the smaller scales in an important extent and so they can be neglected. A clear example are ocean flows, where the necessary resolution to compute a reliable estimate of the velocity structure function is still inaccessible while for tracers such as the SST obtained by remote sensing is rather feasible. According to some studies, the multifractal properties of oceanic barotropic flows are not affected by the presence of baroclinic instabilities [*Abraham and Bowen*, 2002]. As a matter of fact, if a multifractal hierarchy *à la* Parisi & Frisch is evidenced for a given scalar, we will accept that its most plausible origin is the turbulent flow driving the scalar.

Now we have the basic elements to set up the microcanonical formalism and recover dynamical information from the geometrical properties of the flow. Given a scalar signal $s(\vec{x})$, we will say that it is associated to a microcanonical multifractal if and only if:

i) For any point $\vec{x}$,

$$\mathcal{T}_r s(\vec{x}) \sim r^{h(\vec{x})} \quad (16)$$

is verified over a large enough range of scales r, where $\mathcal{T}_r$ is a size-dependent local functional which acts on the variable $s(\vec{x})$ and generalizes equation (15).

ii) The distribution of singularities at any valid scale r follows equation (12), for the same curve $D(h)$.

iii) The curve $D(h)$ derived from equation (12) is convex.

Condition i) means that any point can be assigned to a fractal singularity manifold $\mathcal{F}_h$, so the multifractal decomposition is exhaustive; in addition, as these sets are of fractal nature, i) guarantees that each component is scale invariant. Condition ii) means that the relations among the different members of the hierarchy can be referred to an invariant, the singularity spectrum $D(h)$, so the whole hierarchy is scale-invariant. The third condition is not strictly necessary, but it is important to complete the link with statistics: as the curve $D(h)$ is convex, it coincides with Parisi and Frisch's estimate, equation (14). Hence, the singularity spectrum $D(h)$ exactly corresponds to the multiplicative cascade. This is very relevant for us, because a convex, invariant singularity spectrum is plausibly linked to oceanic turbulence and so it can reasonably be inferred that the observed multifractal is of oceanic origin.

An interesting question is the explicit calculation of the singularity spectrum $D(h)$. Assuming that equation (16) holds in a given range of scales, it allows to calculate the singularity exponent $h(\vec{x})$ associated to each point $\vec{x}$. Then, the empirical histograms, which are directly linked to $D(h)$ (see equation 12), can be used to obtain the singularity spectrum. We proceed in a similar way to what is done in *Turiel et al.* [2006a, b]: as we know that the support of h has maximum dimension d, there exists a fractal component of such a dimensionality, that is, there is a value h_1 such that $D(h_1) = d$. This necessarily corresponds to the mode of the probability distribution, that is the more common value in the empirical histogram of singularities $\rho(h)$. So, we normalize the histogram by its maximum to remove the implicit proportionality constant in equation (12), and so we can retrieve the singularity spectrum from a single scale, in the way:

$$D(h) = d - \frac{\log\left(\frac{\rho(h)}{\rho(h_1)}\right)}{\log r} \quad (17)$$

Condition iii) can be easily verified from the expression above; condition ii) will be verified when the singularity spectra resulting from the application of equation (17) at different scales r are compared together. We are now ready to apply this theoretical framework to satellite SST images and check out its validity in this context.

3. Data

3.1. Pathfinder SST data

In this study we have used daily Pathfinder Sea Surface Temperature (SST) data version 5.0 downloaded from the Physical Oceanography DAAC at JPL (http://podaac.jpl.nasa.gov, product number 216). This dataset is a new reanalysis of the AVHRR data stream developed by the University of Miami's Rosenstiel School of Marine and Atmospheric Science (RSMAS), the NOAA National Oceanographic Data Center (NODC) and NASA's Physical Oceanography Distributed Active Archive Center (PO.DAAC). This reprocessing uses an improved version of the Pathfinder algorithm [e.g. *Kilpatrick et al.*, 2001] and processing steps to produce twice-daily global SST and related parameters back to 1985, at a resolution of approximately 4 km, the highest possible for a global AVHRR data set form NOAA 7, 9, 11, and 14 polar orbiting satellites.

Among the several tests done in this study we have selected two sample images corresponding to ascending passes (day measurements) for the Gulf Stream and the Agulhas current areas in May 8, 2000 and November 26, 2002 respectively; see figure 1. All pixels have been included in our analysis, even those with a quality flag of 0, but excluding those corresponding to land.

3.2. MODIS SST and brightness temperature data

To validate the results obtained using Pathfinder SST, we have also used MODIS Terra L1b and L2 data in the Gulf Stream area corresponding to May 8, 2000 downloaded from

the Goddard Earth Sciences Distributed Active Archive Center (GES-DAAC, http://daac.gsfc.nasa.gov/MODIS/). In particular, long wavelength (11-12μm) SST product (MOD28L2) that combines brightness temperatures from channels 31 and 32 has been used. The geolocated and corrected brightness temperature products (MOD021KM) from channel 31 only (band center 11.03μm; band width: 0.5μm) has also been used, which is the most similar band to AVHRR channel 4 used in previous studies [e.g. *Bowen et al.*, 2002]. No cloud mask was applied in order to have a situation as close as possible to Pathfinder data.

3.3. Altimetric data

For comparison with SST data, in this study we have used Delayed-Time Maps of Sea Level Anomaly (DT-MSLA) produced by Collecte Localisation Satellites (CLS) in Toulouse (France) and distributed by AVISO (Ssalto/Duacs, ftp://ftp.cls.fr/pub/oceano/enact/msla/, *SSALTO/DUACS User Handbook* [2006]), which combine the signal of all available altimeters. These maps are processed including usual corrections (sea-state bias, tides, inverse barometer, etc.) and with improved ERS orbits using *TOPEX/Poseidon* as a reference [*AVISO User Handbook*, 1996; *Le Traon et al.*, 1998]. *TOPEX/Poseidon* has been also used to reduce the contamination of ocean signal variability on the ERS mean prior to the computation of its mean profile [*Ducet et al.*, 2000]. SLA are then regularly produced by subtracting a seven-year mean value (1993-1999) and prior to the analysis, data are low-pass filtered using a Lanczos filter with a cutoff wavelength that depends on latitude in order to reduce altimetric noise [*Ducet et al.*, 2000]. SLA maps are finally built, every 10 days, using an improved space/time objective analysis method, which takes into account long wavelength errors, on a regular grid of $1/3 \times 1/3$ degrees [*Le Traon et al.*, 1998; *Ducet et al.*, 2000]. To have an estimation of the sea surface topography (η) the RIO-03 Combined Mean Dynamic Topography [CMDT, *Rio and Hernández*, 2004] has been added to the maps of SLA.

4. The multifractal structure of SST images

4.1. Singularity analysis

The key element for the application of the microcanonical formalism is the ability to obtain singularity exponents. Equation (15) is very appealing and it is easy to relate to properties of the flow. However, it does not hold in general, because of the existence of long-range correlations in the flow which could mask the softest singularity exponents [*Arneodo et al.*, 1995]. To deal with the existence of such long-range correlations, $s(\vec{x})$ has to be filtered. However, we do not want to impose a fixed scale in the filter which could truncate the range of valid scales or, even worse, which could mask the value of the scaling exponents. Continuous wavelet transforms, defined as projections of the signal at different resolutions, are appropriated to filter multiscaling functions without disturbing scale invariance properties [*Daubechies*, 1992; *Arneodo et al.*, 1995]. According to the derivations presented in *Arneodo et al.* [1995], let us consider a wavelet Ψ capable to vanish any polynomial contribution up to a given order [*Arneodo et al.*, 1995; *Arneodo*, 1996]. Equation (15) has a wavelet-transformed counterpart, in the way:

$$T_\Psi s(\vec{x},r) \;\sim\; r^{\tilde{h}(\vec{x})} \tag{18}$$

where $T_\Psi s(\vec{x},r)$ is the wavelet projection of s over the wavelet Ψ at the point $\vec{x}$ and the scale $r>0$, defined as:

$$T_\Psi s(\vec{x},r) \;\equiv\; \int d\vec{x}'\; s(\vec{x}')\,\frac{1}{r^2}\Psi\left(\frac{\vec{x}-\vec{x}'}{r}\right). \tag{19}$$

$T_\Psi s(\vec{x},r)$ represents a convolution of the signal by a version of the wavelet Ψ re-sized by the scale factor r. Equation (18) has been shown to be fully operative for studying turbulent flows, and has a more general scope than equation (15): equation (15) implies equation (18), but the converse is not true. In fact, equation (18) leads to the same singularity exponents as equation (15) when no long-range correlation is present and can be employed to perform the statistical analysis of the energy cascade [*Muzy et al.*, 1991; *Bacry et al.*, 1993; *Kestener and Arnéodo*, 2003]. However, equation (18) has some numerical problems [*Struzik*, 2000], mainly due to the requirement of using wavelets Ψ with several zero-crossings, what reduces the spatial resolution in the determination of the singularity exponents [*Turiel and Pérez-Vicente*, 2004; *Turiel et al.*, 2006a]. This problem has been solved by processing the modulus of its gradient, $|\nabla s|(\vec{x})$, instead of the signal itself. If the signal is multifractal, the gradient modulus field verifies a relation analogous to equation (18), namely:

$$T_\Psi|\nabla s|(\vec{x},r) \;\sim\; r^{h(\vec{x})} \tag{20}$$

(see, for instance, *Turiel and Parga* [2000]; *Grazzini et al.* [2002]), where the exponents $h(\vec{x})$ are simply related to the exponents $\tilde{h}(\vec{x})$, $h(\vec{x}) = \tilde{h}(\vec{x}) - 1$ [*Daubechies*, 1992; *Turiel and Parga*, 2000; *Kestener and Arnéodo*, 2003]. The advantage of processing gradients instead of signals is that the family of functions Ψ suitable to perform the analysis becomes larger, and in particular positive functions can be employed, what gives a fine resolution [*Turiel and Parga*, 2000]. For this reason we will use equation (20) as the practical implementation of the operator in equation (16).

¿From a theoretical point of view, all wavelets lead to the same singularity exponents [*Daubechies*, 1992]. In fact, all the wavelets lead to very similar results in experimental situations, that is, when applied to discretized data [*Turiel*, 2003]; nevertheless some wavelets may perform better than others. Two questions must be taken into account when choosing a wavelet for analyzing real data. First, the wavelet must be able to discriminate all the singularities in the given range [*Turiel*, 2003; *Turiel and Pérez-Vicente*, 2004], what is related with the tail of the wavelet. Second, the wavelet must allow to access scales as small as possible in order to attain an optimal spatial resolution. This drives the choice to positive wavelets (when they can be employed; for instance, with measures), as the minimum resolution of non-positive wavelets are limited by the number of zero crossings [*Turiel et al.*, 2006a].

A family which has been shown [*Turiel*, 2003; *Turiel et al.*, 2006b] to be the most efficient to attain good discrimination and resolution capabilities is the Lorentzian family, namely:

$$\mathcal{L}_\beta(\vec{x}) = \frac{1}{(1+\vec{x}^2)^\beta}, \quad \beta \geq 1 \tag{21}$$

The best resolution is attained by $\beta = 1$, but $\mathcal{L}_1$ has heavy tails and so it truncates singularities above a given threshold [*Turiel*, 2003; *Turiel et al.*, 2006b]. A simple way to circumvent this difficulty is to define the wavelet by means of appropriate discretized weights which approximate $\mathcal{L}_1$ in the shorter scales and with lighter tails. This wavelet has proved to be very efficient in practice [*Turiel et al.*, 2005b, a, 2006b], attaining good resolution and discrimination capabilities. We will always use this wavelet for the rest of the paper.

4.2. Results

We verify here that the requirements i-iii) defining the microcanonical multifractal formalism are satisfied by Pathfinder SST data. To do that we must explore the degree of accuracy of equation (20) to perform singularity analysis. We have chosen SST images corresponding to the Gulf Stream area and Agulhas current region (figure 1). With these data, the available range of scales to be explored is limited by below due to the finite resolution r_0 (typically, one pixel, ~ 4 km for Pathfinder SST images) and by above due to the finite size (L). Assuming that equation (20) holds, the singularity exponent $h(\vec{x})$ is computed performing a log-log regression on equation (20) (that is a linear regression of $\ln(T_\Psi|\nabla s|(\vec{x},r))$ vs $\ln r$) from r_0 up a valid scale, $r_M < L$. As r_M increases, a decrease in the linear regression coefficient is expected. For each choice of r_M, 21 scaling points are sampled uniformly along the logarithmic axis from $\ln r_0$ to $\ln r_M$. We will consider that equation (20) is valid when the regression coefficient is above 0.9 (in absolute value). We thus define the validity radius at the point $\vec{x}$, $R(\vec{x})$, as the maximum radius r_M foe which equation (20) is valid.

In top row of figure 2 we present the radii $R(\vec{x})$. Equation (20) is found to hold for radius up to 110 pixels for the Gulf stream image and 149 for the Agulhas image (which corresponds to $\sim$441 km and $\sim$596 km respectively). The maximum validity radii are maximal in the central part of the image and decrease close to the image limits and the coast, due to the presence of these boundaries. Regions contaminated by clouds (e.g. bottom left corner of both images) have smaller but non vanishing $R(\vec{x})$. This is because clouds have their own multifractal structure [*Arrault et al.*, 1997; *Turiel et al.*, 2005a] which is, in general, different form cloud-free areas. For that reason, the multifractal hypothesis also holds inside clouds but radii are smaller as clouds are rather small in the studied images.

Having associated a singularity exponent to each point in the image, we can obtain an explicit multifractal decomposition, that is, to assign points to the different fractal components. In addition, we can obtain the empirical estimate of the distribution of singularities at different scales, (conditions ii) and iii)). A visual inspection of the singularity exponents associated to the same images (second row of figure 2) is very revealing. A grey-level representation of the singularity exponents is a possible visualization of the multifractal hierarchy, and this does not only delineate the most obvious patterns in SST images (such as boundary currents and several mesoscale eddies) but also highlights some subtler structures. Notice that the presence of long-range correlations in original SST (for instance, due to the meridional variations of temperature) masks all such small-amplitude structures which are revealed by the enhanced detection capability of singularity analysis, which are independent of the local amplitude.

The empirical probability density function (PDF) of singularity exponents are unimodal (figure 3) and we obtain convex singularity spectra $D(h)$ when equation (12) is applied. When the singularity spectra arising from different minimum scales are compared, we still obtain essentially the same convex curve for all the images analyzed (not shown) so validating its scale-invariant character.

One may wonder if the rich picture of exponents revealed by the singularity analysis can be affected by, or even be, the result of noise contamination in the algorithm used to get the SST images. It has been noticed [*Bowen et al.*, 2002] that, when tracking oceanic structures, Brightness Temperatures (BT) as recorded by some infrared channels leads to better results than the multichannel derived SST image. This has been attributed to a possible increased influence of noise due to the AVHRR algorithm (NLSST, *Walton et al.* [1998]), as it based on the difference of temperatures from AVHRR channels 4 and 5. In Figure 5 we compare the singularity analysis for a SST image and the corresponding BT, both from MODIS. The analysis over the BT gives better results with an improved discrimination over subtler patterns, although the SST image also allows to recover the main mesoscale features. However, when the analysis is done over MODIS SST and BT images reduced (by pixel averaging) to a resolution equivalent to that of Pathfinder, both analysis provides almost indistinguishable results. If now we compare with the Pathfinder SST image we can appreciated that results are equally good for singularity detection as BT ones (compare Figure 2, bottom left, with Figure 5, bottom). So far, noise effects are important at the resolution of MODIS images and when working with them the choice should be shifted to BT images. However, for the scope of the results here presented Pathfinder images perform almost equally well.

Another important issue is the oceanic origin of the observed multifractal structure. Infrared signals may be contaminated by atmospheric conditions that themselves also have multifractal properties. Figure 4 presents a sequence of exponent images obtained during several days in a large area around the Gulf Stream. As it can be observed from the figure, many structures (indeed the Gulf Stream signature itself, but also some mesoscale eddy-like structures) can be recognised during several days. The structures evolve slowly (in the scale of days), according to a plausible oceanic origin compatible with mesoscale dynamics which is not likely for any atmospheric feature having in general shorter characteristic times. Certainly, the presence of clouds introduces occlusion and some perturbation on the neighbouring areas, but due to the local character of the singularity exponents this type of perturbations are short-ranged compared to the textures in the oceanic regions.

We can therefore state that SST images verify all the requirements of the Microcanonical Multifractal Formalism which confirms its multifractal structure within the range of available scales. Due to the existence of a multifractal hierarchy, the most probable origin of the observed structures is the turbulent character of the oceanic flow. In addition, the applied singularity analysis provides an spectra of singularity exponents which looks similar even for different regions (see Figure 3) suggesting that the underlying processes leading to the multifractal structure are of similar nature. Different phenomena acting significantly on the system would lead to a non-convex empirical $D(h)$.

5. The Maximum Singularity sreamfunction method

Results in previous section lead to decompose the signal into different patterns (called singularity or fractal components), each one characterized by a value of the singularity exponents $h(\vec{x})$. The components can be classified from the most singular (associated to sharp transitions in the signal) to the less singular, associated to smooth, continuous areas [*Turiel and Parga*, 2000]. As a matter of fact, one of the main advantages of multifractal formalism is the lack of any continuity requirement on the signal; even more, some of the fractal components are associated to discontinuities and sharp transitions [*Arrault et al.*, 1997; *Turiel and Parga*, 2000].

5.1. The Most Singular Manifold as the set of main streamlines

The most singular points in the multifractal hierarchy are of great interest because of their dynamical and statistical properties. According to theory the Most Singular Manifold (MSM), that will be denoted as $\tilde{F}_\infty$, is given by

$$\tilde{F}_\infty \equiv \{\vec{x} \ : \ h(\vec{x}) = h_\infty\}, \tag{22}$$

where h_∞ is the most singular exponent, that is, the minimum observed value of singularity [*Turiel et al.*, 1998; *Turiel and Parga*, 2000]. This definition is however too restrictive in practice, because there is an implicit assumption of homogeneity in the multifractal structure. Quite often, however, the signals under analysis extend over regions consisting of different areas, each one dominated by different structures and separated by circulation barriers. In such cases, although each part has a multifractal character, they do not necessarily have the same multifractal structure with exactly the same multifractal parameters, and in particular h_∞ needs not to be the same all over that region. To overcome these difficulties the MSM is extended to a coarser version. For our work, the MSM, now denoted F_∞, will be given by:

$$F_\infty \equiv \{\vec{x} \ : \ h(\vec{x}) < h_0\}, \tag{23}$$

where h_0 is the most probable value. This definition is a coarse graining of the actual MSMs but fully operational in practice and for the scope of this paper we will employ it.

From the statistical point of view, the MSM has been related with the vertex of the energy cascade in turbulence [*She and Leveque*, 1994]. In 2D decaying turbulence studies it is observed that there exist a tendency towards an alignment of passive tracer gradients and vorticity gradients (active tracer) [*Lapeyre et al.*, 2001]. From the dynamical point of view, it has been experimentally shown that the multifractal structure of reactive tracers is essentially the same as that of passive tracers [*Abraham and Bowen*, 2002], what has allowed to conclude that singularities are mainly advected by the flow, a fact which is consistent with the known theory [*Frisch*, 1995]. Bearing this in mind, each fractal component of the tracer field can be regarded as the union of some instantaneous stream-lines. An experimental evidence is that observed fractal components in fluids have dimensions greater than 1 [*Turiel and Parga*, 2000; *Grazzini et al.*, 2002; *Turiel et al.*, 2005a, b], what is consistent with having components consisting in streamlines. Separating each one of these stream-lines from a higher dimension fractal component is very complicated, and can only be done without imposing further requirements when the dimension of the component is exactly equal to 1. This is precisely the case for the MSM, what allows to recognize the main stream-lines in the flow. Furthermore, the MSM is associated to the largest order singularities, so the stream-lines associated are likely those inducing the strongest shear.

5.2. sreamfunction reconstruction from the MSM

Once the MSM is associated to the main instantaneous stream-lines of the flow we can recover the velocity field from the scalar images. In general for a given distribution of the gradient of a signal, the SST in our case, defined only over the MSM, there is an algorithm relying on the statistical properties of FDT which allows to regenerate a divergence-free field which coincides with the starting data on the MSM and which is compatible with some basic statistical requirements [*Turiel and del Pozo*, 2002]. Indeed, in this algorithm, the input data are the values of the gradient of the signal over the MSM, and the reconstruction is performed by means of a linear vectorial kernel $\vec{g}$. The reconstructing kernel is completely defined when some requirements are imposed. These requirements are the following: determinism, linearity, statistical translational invariance, statistical isotropy and compatibility with the known shape for the power spectrum. The reconstruction algorithm has shown to be of great quality in different applications, including image processing [*Turiel and del Pozo*, 2002], analysis of meteorological images [*Grazzini et al.*, 2002; *Turiel et al.*, 2005b] and time-series analysis [*Turiel and Pérez-Vicente*, 2003, 2005].

Given a multifractal signal, in this case the sreamfunction of the flow $\psi(\vec{x})$, we denote $\nabla_\infty\psi$ as the vector field of gradients restricted to the MSM only, that is,

$$\nabla_\infty\psi(\vec{x}) \ \equiv \ \nabla\psi(\vec{x})\delta_\infty(\vec{x}) \tag{24}$$

where $\delta_\infty(\vec{x})$ means a delta-like function defined over F_∞ (so it gives contributions on F_∞ only). The reconstruction algorithm [*Turiel and del Pozo*, 2002] is given by:

$$\psi \ = \ \vec{g} \otimes \nabla_\infty\psi \tag{25}$$

where the symbol $\otimes$ stands for the convolution dot product,

$$\vec{g} \otimes \nabla_\infty\psi \equiv g_x * \left.\frac{\partial\psi}{\partial x}\right|_\infty + g_y * \left.\frac{\partial\psi}{\partial y}\right|_\infty, \tag{26}$$

and $*$ is the standard convolution product. The reconstructing kernel $\vec{g}$ has a very simple functional shape. In Fourier space it reads:

$$\hat{\vec{g}}(\vec{k}) = \frac{i\vec{k}}{k^2}, \tag{27}$$

where $\vec{k}$ is the wave vector. Taking into account that the gradient of the sreamfunction must be perpendicular to the stream-lines and that in fact $\nabla\psi = \vec{e}_z \times \vec{v}$ ($\vec{e}_z$ is the normal vector perpendicular to the xy plane), the reconstruction formula, equation (25), can be written in terms of the velocity over the MSM ($\vec{v}_\infty$) as:

$$\psi = \vec{g} \otimes (\vec{e}_z \times \vec{v}_\infty) \tag{28}$$

The stream-lines forming the MSM give information about the directions of the velocity vectors, but not about their moduli or sense, which implies that they need to be independently defined. The velocities over the MSM can be written as

$$\vec{v}_\infty \ = \ \xi_\infty U_\infty \vec{v}^*_\infty \tag{29}$$

where U_∞ is the modulus of the velocity, ξ_∞ the sign and $\vec{v}^*_\infty(\vec{x})$ is a non-dimensional velocity field with modulus 1 and the same sense of the velocities than that of the gradient of s rotated counter-clockwise 90 degrees, that is, velocity is made to point to the same side as $\nabla s(\vec{x}) \times \vec{e}_z$. The quantities U_∞ and ξ_∞ must be given by some extra, external source, as the analysis so far is geometric and do not allow to retrieve them. In *Turiel et al.* [2005b] it was proposed the simplest possible guess for these quantities:

$$U^M_\infty \ = \ \xi^M_\infty \ = \ 1 \tag{30}$$

This guess is a natural extension of the thermal wind hypothesis, as it states that the sense (but not the direction) of the velocity comes from the one induced by the SST gradient. When this guess is substituted in equation (29), the function $\psi_M(\vec{x})$ resulting from the application of equation (28), is known as the Maximum Singularity sreamfunction (MSS), first introduced in *Turiel et al.* [2005b].

5.3. Results

¿From the computation of the singularity exponents of SST images, the MSM (identified with the main streamlines) has been extracted using a threshold $h_0 = 0.2$. This value has been selected because it represents a compromise between capturing as much patterns as possible but keeping the MSM lines as thin as possible. To show how the choice affects the captured sets, in figure 6 we plot the resulting MSM using several values of the threshold for the Gulf Stream region. The threshold controls the number of structures retained in the image. As the value of the singularity threshold is decreased, the retained points correspond to the sharpest gradients of the image, which are associated to a mixture of ocean thermal fronts, land-water transitions and cloud boundaries. A too small value of h_0 would excessively filter some coherent fronts, which are put in evidence as h_0 approaches the most probable value (compare the images for $h_0 = 0$ and $h_0 = 0.1, 0.2$) and then, as h_0 goes on increasing the MSM becomes thicker and thicker. Although the MSM should represent streamlines, numerical limitations and data resolution may force some lines to end within the flow or intersect between them. Another important aspect concerns the effect of land-water transitions and cloud contaminated pixels. Land-water transitions are step-like (as no value is assigned to the pixels on land) and so the MSM aligns with the coastline. This part of the MSM acts as a fictitious parallel current which actually represents the boundary condition at the coast. This is very useful, as it allows treating coasts with the same reconstruction formula and produce sreamfunctions with the correct boundary conditioning. A somewhat different situation appears with clouds. Clouds are complex structures with their own inner singularity organization and for that reason some exponents are detected inside. However, the cloud-water transition behaves in a fashion much similar to the coastline, so inducing an extra boundary condition (as if the cloud was an island; see figure 2, third row, where their lower-left corner is contaminated by clouds). In this case the effect is not beneficial as for coasts, as it distorts the actual flow course. However, this boundary condition guarantees a short range perturbation of the MSS and hence the influence of the clouds is kept rather controlled in space (contrary to what happens with other methods).

The computation of ψ_M from SST is straightforward (Figure 7). It provides an field with the same resolution as the original SST image but in contrast, the MSS field reveals a rich structure of eddies, fronts and similar features. A qualitative comparison between the MSS and an independent estimation of the streamfunction can be made just by over-plotting the sea level anomaly η from altimetry to ψ_M (Figure 7). A good correspondence between the isolines of the MSS and η can be observed. In particular, there is a good matching between mesoscale eddies and other structures from one field to the other in Gulf Stream image, a bit worse in the case of Agulhas image. Notice that the MSS contains a much richer structure due to its greater spatial resolution. In some specific areas, sea level contours are not co-located with MSS lines but cross them with a high angle (see for example the area close to the point 40^o S, 23^o E). However, when comparing with altimetry it is important to take into account that sea level is measured only on satellite tracks and an interpolation method have been used to recover the 2D field. Recently, it has been shown that if only two altimeters are used, which is the case of the altimetry data here used, there might be some erroneous reconstruction of ocean flow patterns [*Pascual et al.*, 2006].

In spite of the general good correspondence between both fields, there are other qualitative differences. For the Gulf Stream image, the Gulf Stream appears as a tube-like structure (higher values of ψ_M in the center of the stream decreasing towards the borders) instead of the step-like shape (monotonic increase of the sreamfunctions towards the South) that can be observed in altimetric maps. To shed some light on this phenomenon, Figure 8 shows the vector field associated to the MSS, $\vec{v}^*_\infty$, for a small area centered over the Gulf Stream jet. ¿From the figure it is evident that velocities have opposite senses in the meridional boundaries of the stream, which can be easily identified as the void region bounded by the MSS along the diagonal of figure 8 (see also figures 2 and 6). The lack of internal thermal structure within the jet leads the sreamfunction reconstruction using $\xi_\infty = 1$, to have a tube-like structure instead of step-like. The origin of this erroneous determination of the sign of $\vec{v}^*_\infty$ is the pointing of velocities in the direction derived from the gradients of the SST. However, notice that when deriving ψ_M from SST it will be a good approximation to the actual ψ if temperature gradient points in the same sense as the density gradient.

6. Integration external data sources: the case of altimetry

As shown in the previous section the MSM is essentially a geometric method very precise and useful to put in evidence structures hidden in the original SST. The inferred ψ_M is a first approximation to the real streamfunction that has some limitations, in particular cannot retrieve correct values of U_∞ and ξ_∞ and may fail in some cases to reproduce the velocity field related to some areas. This can be overcome by integrating additional independent information on the velocity field. Let us suppose that we have velocity measurements coming from other devices (Lagrangian floats, current-meters, ADCP measurements, etc.) that provide information over some points of the MSM. Let us denote by $\vec{v}_{i,\infty}$ such velocity field. Now, U_∞ and ξ_∞ can be simply evaluated using $\vec{v}_{i,\infty}$ through

$$U^i_\infty = \|\vec{v}_{i,\infty}\| \tag{31}$$

and

$$\xi^i_\infty = \frac{\vec{v}_{i,\infty} \cdot \vec{v}^*_\infty}{|\vec{v}_{i,\infty} \cdot \vec{v}^*_\infty|} \tag{32}$$

As an example, we will use geostrophic velocities derived from altimetry to improve the results of the previous section. This is an interesting case because altimeters provide much more information compatible with the spatial coverage of an SST image and, from an operational point of view, being both satellite data the combination can be done in a routine way.

Given the sea surface topography $\eta(\vec{x})$, a velocity field can be estimated through the geostrophic approximation

$$\vec{v}_\eta(\vec{x}) = \vec{e}_z \times \frac{g}{f_0} \nabla\eta(\vec{x}) \tag{33}$$

where f_0 is the Coriolis parameter at a reference latitude and g the gravity. The geostrophic sreamfunction, denoted by $\psi_\eta(\vec{x})$, is defined as:

$$\psi_\eta(\vec{x}) = \frac{g\eta(\vec{x})}{f_0} \tag{34}$$

Now, introducing $\psi_\eta(\vec{x})$ in 31 and 31 we can recompute ξ^η_∞ and U^η_∞. In Figure 9 we have presented these fields . The value of ξ^η_∞ may change from one to another line of

the MSM, but it is consistently constant along each streamline. More interestingly, the figures show that U_∞^η is almost constant or changes smoothly along the MSS lines in the Gulf Stream region; for the Agulhas area the U_∞^η evolves smoothly during shorter segments due to the worse agreement between altimetry and SST. Figure 10 plots the same zoom of the velocity field over the MSS than figure 8 but with the calibrated velocities ($\vec{v}_\infty^\eta$) instead of the non-dimensional ones ($\vec{v}_\infty^*$). From this figure it is evident not only the variation of speed but the change of the sign of velocities in the southern boundary of the Gulf Stream. Figure 11) shows the sreamfunction (ψ_η) integrating the additional information. Stream-lines are almost compatible with those from ψ_M (as both have been derived from the same MSM) but in this case given a correcting the right direction more consistent with the known shape of the Gulf Stream. To finish, let us remark that the scheme used here to incorporate additional information in order to improve the streamfuction is general and can be applied without changes to include direct in situ velocity measurements of velocity coming from any device.

7. Conclusions

In the first part of the paper we have shown that the thermal structures observed in SST images (Pathfinder SST) exhibit a multifractal structure according to what it is expected for a turbulent flow. A singularity analysis has been carried out to compute the scaling exponents associated to the thermal gradients over the range of available scales in the images. The spectrum of singularity exponents satisfies the expected properties of multifractality found in fully developed turbulent flows. We have observed this for a time series of images over the same area and for two different areas, and in all cases we obtained roughly the same singularity spectra. This fact could be related to the existence of common mechanism in the generation of oceanic thermal structures at the mesoscale, although much more systematic analysis over a greater set of images needs to be done in order to prove it.

The singularity analysis confirms that SST images satisfy the microcanonical multifractal formalism, which allows to assign anomalous scaling exponents not only for global statistical properties of the field, as it is common in the literature on turbulence studies, but to assign it to each point of the analyzed data. The singularity analysis applied to the SST images have revealed a very rich structure of patterns not evident from a look into the original image, so working as an efficient edge detector. Another consequence of this analysis is that the field can be separated in fractal components, depending of the exponents values, which have a direct translation in classifying data points in sets. The most relevant set is associated to the most singular exponent, the so-called the Most Singular Manifold, MSM. The MSM for SST images studied here is associated to sharp thermal fronts, not necessarily intense at a global scale but at a local scale.

In the second part of the paper, the extraction of the MSM from the SST images has been used to infer the most informative streamlines, the Maximum Singular sreamfunction denoted as the MSS method. Thus, an ocean velocity field over these streamlines can thus be obtained from a single image. The crucial step here is to assume that the MSM is related with the instantaneous sreamfunction because the singularities are mainly advected by the flow. Despite of a formal proof is needed, the results confirms that the obtained field is very reasonable and comparable with for example the sea level anomaly field from altimetry. However, although based on general considerations on the statistical properties of the flow, the method is essentially geometric as no specific dynamical information of the system under study is included. Since the direction of the velocity has to be tangent to the streamlines, it can be obtained from the method itself. But the modulus and sign of these velocities remain undetermined. A first choice to solve this is to arbitrarily fix the modulus of the velocity to 1 and derive the sign from the sign of the tracer gradient. Although this does not provide the correct sreamfunction everywhere, it has the effect of enhancing the structures present in SST images. Alternatively, we have shown that a simple scheme can be built to include additional information on the velocity field. Any independent measurement or estimate of the velocity on the main streamlines (Lagrangian drifters, current-meters, etc.) can be integrated within the MSS method. Here, the case of incorporating the geostrophic velocities derived from altimetry has been applied leading to a streamfunction that reproduce much more correctly some undetermined features of the realistic sreamfunction. Thus the MSS method may potentially be used to improve the existing altimetric maps, providing higher resolution estimates of the geostrophic stream function or even to include dynamical constrains such as ones recently implemented to analyze microwave SST *Lapeyre and Klein* [2006]; *Isern-Fontanet et al.* [2006a].

Finally, the MSS method can be used as an alternative to other methodologies developed in the past to infer motion from satellite images [i.e. *Horn and Schunk*, 1981; *Emery et al.*, 1986; *Kelly*, 1989; *García and Robinson*, 1989; *Whal and Simpson*, 1991; *Wu et al.*, 1992; *Kuo and Yan*, 1994; *Côté and Tatnall*, 1995; *Afanasyev et al.*, 2002; *Bowen et al.*, 2002]. Roughly speaking, these methods obtain the velocity field through a matching algorithm of contour patterns, edges or correlation analysis between windowed regions of sequential images. In contrast, the major benefits of the MSS method is that the streamfunction is obtained from a single image and with same resolution as the original SST image. In addition, as far as the hypothesis of multifractality is satisfied images of any other tracer; for example, ocean color images from visible sensors should be equally valid for retrieving the MSS. In many situations the SST may not be a sufficient representative of the underlying flow. In such case the information provided by visible sensors, which is an integration over the first meters of the ocean, may reflect better the flow of the upper layer of the ocean.

Acknowledgments. This is a contribution to the EU MERSEA project (AIP3-CT-2003-502885) and to the Spanish projects ESEOO (VEM2003-20577-C14-10) and MIDAS-4 (ESP2005-06823-C05-1). A. Turiel is funded by a Ramon y Cajal fellowship from the Spanish Ministry of Education. The AVHRR Oceans Pathfinder SST data were obtained from the Physical Oceanography Distributed Active Archive Center (PO.DAAC) at the NASA Jet Propulsion Laboratory, Pasadena, CA. The altimeter products were produced by the CLS Space Oceanography Division as part of the Environment and Climate EU ENACT project (EVK2-CT2001-00117) and with support from CNES. We would like to thank the contribution of the anonymous revieweres that strongly helped to improve the clarity and focus of the paper.

References

Abraham, E., and M. Bowen (2002), Chaotic stirring by a mesoscale surface-ocean ow, *Chaos*, *12*(2), 373–381.

Afanasyev, Y. D., A. G. Kostianoy, A. G. Zatsepin, and P. Poulain (2002), Analysis of velocity field in the eastern black sea from satellite data during the black sea's experiment, *Journal of Geophysical Research*, *107*(0), 10.1029/2000JC000,578.

Amaral, L. A. N., A. L. Goldberger, P. C. Ivanov, and H. E. Stanley (1998), Scale-independent measures and pathologic cardiac dynamics, *Physical Review Letters*, *81*(11), 2388–2391.

Arneodo, A. (1996), Wavelet analysis of fractals: from the mathematical concepts to experimental reality, in *Wavelets. Theory and applications*, edited by G. Erlebacher, M. Y. Hussaini, and L. Jameson, p. 349, Oxford University Press. ICASE/LaRC Series in Computational Science and Engineering, Oxford.

Arneodo, A., F. Argoul, E. Bacry, J. Elezgaray, and J. F. Muzy (1995), *Ondelettes, multifractales et turbulence*, Diderot Editeur, Paris, France.

Arneodo, A., et al. (1996), Structure functions in turbulence, in various flow configurations, at reynolds number between 30 and 5000, using extended self-similarity, *Europhysics Letters*, *34*(6), 411–416.

Arrault, J., A. Arneodo, A. Davis, and A. Marshak (1997), Wavelet-based multifractal analysis of rough surfaces: application to cloud models and satellite data, *Phys. Rev. Lett.*, *79*, 75–79.

AVISO User Handbook (1996), *Corrected Sea Surface heights products*, 2.0 ed., aVI-NT-011-311-CN.

Bacry, E., J. F. Muzy, and A. Arneodo (1993), Singularity spectrum of fractal signals from wavelet analysis: exact results, *J. of Stat. Phys.*, *70*, 635–673.

Bowen, M., W. Emery, J. Wilkin, P. Tildesley, I. Barton, and R. Knewtson (2002), Extracting multiyear surface currents from sequential thermal imagery using the maximum cross-correlation technique, *Journal of Atmospheric and Oceanic Technology*, *19*(10), 1665–1676.

Carleman, T. (1922), Sur le problème des moments, *Comptes rendus Acad. Sci. Paris*, *174*, 1680.

Chapron, B., F. Collard, and F. Ardhuin (2005), Direct measurement of ocean surface velocity from space: Interpretation and validation, *J. Geophys. Res.*, *110*, doi:10.1029/2004JC0022.

Chhabra, A., C. Meneveau, R. Jensen, and K. Sreenivasan (1989), Direct determination of the f(*alpha*) singularity spectrum and its application to fully developed turbulence, *Physical Review A*, *40*(9), 5284–5294.

Chigirinskaya, Y., D. Schertzer, S. Lovejoy, A. Lazarev, and A. Ordanovich (1994), Unified multifractal atmospheric dynamics tested in the tropics part 1: horizontal scaling and self organized criticality, *Nonlinear Processes in Geophysics*, *1*, 105–114.

Côté, S., and A. Tatnall (1995), The hopfield neural network as a tool for feature tracking and recognition from satellite sensor images, *International Journal of Remote Sensing*, *18*(4), 871–885.

Daubechies, I. (1992), *Ten lectures on wavelets*, CBMS-NSF Series in Ap. Math., Capital City Press, Montpelier, Vermont.

Davis, A., A. Marshak, and W. Wiscombe (1994), Wavelet based multifractal analysis of non-stationary and/or intermittent geophysical signals, in *Wavelets in Geophysics*, edited by E. Foufoula-Georgiou and P. Kumar, pp. 249–298, Academic Press, New York.

Ducet, N., P. Le Traon, and G. Reverdin (2000), Global high-resolution mapping of ocean circulation from TOPEX/Poseidon and ERS-1 and -2, *J. Geophys. Res.*, pp. 19,477–19,498.

Emery, W., A. Thomas, M. Collins, W. Crawford, and D. Mackas (1986), An objective method for computing advective surface velocities from sequential infrared satellite images, *Journal of Geophysical Research*, *91*, 12,865–12,878.

Falconer, K. (1990), *Fractal Geometry: Mathematical Foundations and Applications*, John Wiley and sons, Chichester.

Frisch, U. (1995), *Turbulence*, Cambridge Univ. Press, Cambridge MA.

García, C. A. E., and I. Robinson (1989), Sea surface velocities in shallow seas extracted from sequential coastal Zone Color Scanner satellite data, *Journal of Geophysical Research*, *94*(C9), 12,681–12,691.

Gille, S., and S. L. Smith (2000), Velocity probability density functions from altimetry, *Journal of Physical Oceanography*, pp. 125–136.

Grazzini, J., A. Turiel, and H. Yahia (2002), Entropy estimation and multiscale processing in meteorological satellite images, in *Proc. of ICPR 2002*, vol. 3, pp. 764–768.

Gupta, V., and E. Waymire (1990), Multiscaling properties of spatial rainfall and river flow distributions, *Journal of Geophysical Research*, *95*(D3), 1999–2009.

Horn, B., and B. Schunk (1981), Determining optical flow, *Artificial Intelligence*, *17*, 185–203.

Hunt, J., O. Phillips, and D. Williams (Eds.) (1991), *Turbulence and stochastic processes: Kolmogorov's ideas 50 years on*, *Proc. Roy. Soc. London Ser. A*, vol. 434, The Royal Society of London.

Isern-Fontanet, J., García-Ladona, and J. Font (2003), Identification of marine eddies from altimetry, *J. Atmos. Oceanic Technol.*, *20*, 772–778.

Isern-Fontanet, J., B. Chapron, G. Lapeyre, and P. Klein (2006a), Potential use of microwave Sea Surface Temperatures for the estimation of ocean currents, submitted to Geophysical Research Letters.

Isern-Fontanet, J., García-Ladona, and J. Font (2006b), The vortices of the Mediterranean sea: an altimetric viewpoint, *J. Phys. Oceanogr.*, *36*, 87–103.

Isern-Fontanet, J., García-Ladona, J. Font, and A. García-Olivares (2006c), Non-gaussian velocity Probability Density Functions: an altimetric perspective of the Mediterranean sea, *J. Phys. Oceanogr.*, submitted.

Ivanov, P., L. Amaral, A. Goldberger, S. Havlin, M. Rosenblum, Z. Struzik, and H. Stanley (1999), Multifractality in human heartbeat dynamics, *Nature*, *399*, 461–465.

Kelly, K. A. (1989), An inverse model fro near-surface velocity from infrared images, *Journal of Physical Oceanography*, *19*, 1845–1864.

Kestener, P., and A. Arnéodo (2003), Three-dimensional wavelet-based multifractal method: The need for revisiting the multifractal description of turbulence dissipation data, *Phys. Rev. Lett*, *91*(19), 194,501, doi:10.1103/PhysRevLett.91.194501.

Kilpatrick, K., G. Podestá, and R. Evans (2001), Overview of the NOAA/NASA advanced very high resolution radiometer Pathfinder algorithm for the sea surface temperature and associated matchup database, *J. Geophys. Res.*, *106*, 9179–9197.

Kolmogorov, A. N. (1941a), The local structure of turbulence in an incompressible fluid with very large reynolds number, *Dokl. Akad. Nauk. SSSR*, *309*, 301–305.

Kolmogorov, A. N. (1941b), Dissipation of energy in a locally isotropic turbulence, *Dokl. Akad. Nauk. SSSR*, *32*, 16–18.

Kuo, N. J., and C. Yan (1994), Using the shape-matching method to compute sea-surface velocities from avhrr satellite images, *IEEE Transactions on Geoscience and Remote Sensing*, *32*(3), 724–728.

Lapeyre, G., and P. Klein (2006), Dynamics of the upper oceanic layers in terms of surface quasigeostrophy theory, *J. Phys. Oceanogr.*, *36*, 165–176.

Lapeyre, G., B. Hua, and P. Klein (2001), Dynamics of the orientation of active and passive scalars in two-dimensional turbulence, *Physisc of Fluids*, *13*, 251–264.

Le Traon, P., and F. Ogor (1998), ERS-1/2 orbit improvement using TOPEX/POSEIDON: the 2cm challenge, *J. Geophys. Res.*, *103*(C4), 8045–8057.

Le Traon, P., F. Nadal, and N. Ducet (1998), An improved mapping method of multisatellite altimeter data, *J. Atmos. Oceanic Technol.*, *15*(2), 522–534.

Llewellyn Smith, S., and S. Gille (1998), Probability density functions of large-scale turbulence in the ocean, *Physical Review Letters*, *81*(23), 5249–5252.

Lovejoy, S., W. Currie, Y. Tessier, M. Claereboudt, E. Bourget, J. Roff, and E. Schertzer (2001), Universal multifractals and ocean patchiness: phytoplankton, physical fields and coastal heterogeneityp, *J. Plankt. Res.*, *23*(2), 117–141.

Meneveau, C., and K. Sreenivasan (1991), The multifractal nature of turbulent energy dissipation, *J. Fluid Mech.*, *224*, 429–484.

Morrow, R., F. Birol, D. Griffin, and J. Sudre (2004), Divergent pathways of cyclonic and anti-cyclonic ocean eddies, *Geophys. Res. Lett.*, *31*, doi:10.1029/2004GL020974.

Munk, W. (2000), Oceanography before, and after, the advent of satellites, in *Satellites, Oceanography and Society*, edited by D. Halpern, pp. 1–4, Elsevier Oceanography Series, Elsevier.

Muzy, J. F., E. Bacry, and A. Arneodo (1991), Wavelets and multifractal formalism for singular signals: Application to turbulence data, *Physical Review Letters*, *67*, 3515–3518.

Novikov, E. A. (1994), Infinitely divisible distributions in turbulence, *Physical Reviev E*, *50*, R3303.

Parisi, G., and U. Frisch (1985), On the singularity structure of fully developed turbulence, in *Turbulence and Predictability in Geophysical Fluid Dynamics. Proc. Intl. School of Physics E. Fermi*, edited by M. Ghil, R. Benzi, and G. Parisi, pp. 84–87, North Holland, Amsterdam.

Pascual, A., Y. Faugre, G. Larnicol, and P. LeTraon (2006), Improved description of the ocean mesoscale variability by combining four satellite altimeters, *Geophys. Res. Lett*, *33*(2), 611, doi: 10.1029/2005GL024.

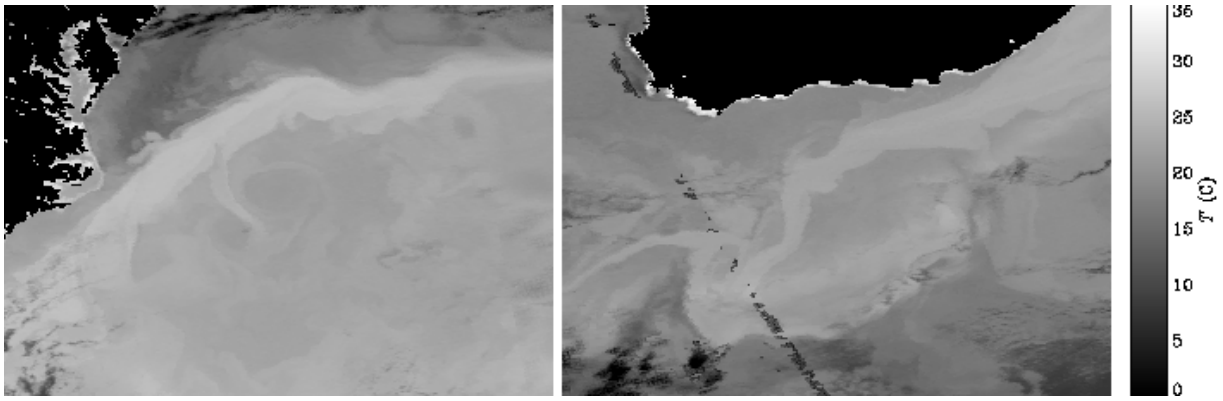

Figure 1. Pathfinder SST images of the Gulf Stream area for May 8 2000 (left) and the Agulhas current area for November 26 2002 (right).

Rio, M.-H., and F. Hernández (2004), A mean dynamic topography computed over the world ocean from altimetry, in-situ measurements and a geoid model, *J. Geophys. Res.*, doi: 10.1029/2003JC002226.

Sachs, D., S. Lovejoy, and D. Schertzer (2002), The multifractal scaling of cloud radiances from 1 m to 1 km, *Fractals*, *10*(3), 1–12.

She, Z. S., and E. Leveque (1994), Universal scaling laws in fully developed turbulence, *Physical Review Letters*, *72*, 336–339.

She, Z. S., and E. C. Waymire (1995), Quantized energy cascade and log-poisson statistics in fully developed turbulence, *Physical Review Letters*, *74*, 262–265.

Sreenivasan, K. (1991), Fractals and multifractals in fluid turbulence, *Ann. Rev. Fluid. Mech.*, *23*, 539–600.

SSALTO/DUACS User Handbook (2006), *(M)SLA and (M)ADT Near-Real Time and Delayed Time Products*, 1rev4 of the 31 january 2006 ed., sALP-MU-P-EA-21065-CLSA.

Struzik, Z. R. (2000), Determining local singularity strengths and their spectra with the wavelet transform, *Fractals*, *8*(2), 163–179.

Turiel, A. (2003), Relevance of multifractal textures in static images, *Electronic Letters on Computer Vision and Image Analysis*, *1*(1), 35–49.

Turiel, A., and A. del Pozo (2002), Reconstructing images from their most singular fractal manifold, *IEEE Trans. on Im. Proc.*, *11*, 345–350.

Turiel, A., and N. Parga (2000), The multi-fractal structure of contrast changes in natural images: from sharp edges to textures, *Neural Computation*, *12*, 763–793.

Turiel, A., and C. Pérez-Vicente (2003), Multifractal geometry in stock market time series, *Physica A*, *322*, 629–649.

Turiel, A., and C. Pérez-Vicente (2004), Multifractal measures: definition, description, synthesis and analysis. a detailed study, in *Proceedings of the "Journées d'étude sur les méthodes pour les signaux complexes en traitement d'image"*, edited by J.-P. Nadal, A. Turiel, and H. Yahia, pp. 41–57.

Turiel, A., and C. Pérez-Vicente (2005), Role of multifractal sources in the analysis of stock market time series, *Physica A*, *355*, 475–496.

Turiel, A., G. Mato, N. Parga, and J. P. Nadal (1998), The self-similarity properties of natural images resemble those of turbulent flows, *Physical Review Letters*, *80*, 1098–1101.

Turiel, A., J. Grazzini, and H. Yahia (2005a), Multiscale techniques for the detection of precipitation using thermal ir satellite images, *IEEE Geoscience and Remote Sensing Letters*, *2*(4), doi:10.1109/LGRS.2005.852712.

Turiel, A., J. Isern-Fontanet, E. García-Ladona, and J. Font (2005b), Multifractal method for the instantaneous evaluation of the stream function in geophysical flows, *Physical Review Letters*, *95*(10), 104,502, doi:10.1103/PhysRevLett.95.104502.

Turiel, A., C. Pérez-Vicente, and J. Grazzini (2006a), Numerical methods for the estimation of multifractal singularity spectra on sampled data: a comparative study, *Journal of Computational Physics*, *216*(1), 362–390.

Turiel, A., H. Yahia, and C. Pérez-Vicente (2006b), Microcanonical multifractal formalism: a powerful approach to image and signal processing, submitted to Multiscale Modeling and Simulation.

Vigan, X., C. Provost, R. Bleck, and P. Courtier (2000a), Sea surface velocities from sea surface temperature image sequences 1. method and validation using primitive equation model output, *Journal of Geophysical Research*, *105*, 19,499–19,514.

Vigan, X., C. Provost, and P. Podesta (2000b), Sea surface velocities from sea surface temperature image sequences 2. application to the brazil-malvinas confluence area, *Journal of Geophysical Research*, *105*, 19,515–19,534.

Walton, C. C., W. G. Pichel, F. J. Sapper, and D. A. May (1998), The development and operational application of nonlinear algorithms for the measurement of sea surface temperatures with noaa polar-orbiting environmental satellites, *Journal of Geophysical Research*, *103*, 27,999–28,012.

Waugh, D., E. Abraham, and M. Bowen (2006), Spatial variations of stirring in the surface ocean: A case study of the Tasman sea, *J. Phys. Oceanogr.*, submitted.

Whal, D. D., and J. J. Simpson (1991), Satellite derived estimates of the normal and tangential components of near-surface flow, *International Journal of Remote Sensing*, *12*, 2529–2571.

Wu, Q. X., D. Pairman, S. J. McNeill, and E. J. Barnes (1992), Computing advective velociites from satellite images of sea surface temperature, *IEEE Transactions on Geoscience and Remote Sensing*, *30*(1), 166–176.

J. Isern-Fontanet, Departement d'Océanographie Physique et Spatiale IFREMER Centre de Brest, Technôpole de Brest-Iroise, BP 70 F-29280 Plouzané, France. (jisern@ifremer.fr)

A. Turiel, Grup d'Oceanografia Física, Institut de Ciències del Mar (CSIC), Passeig Marítim de la Barceloneta 37-49, E-08003 Barcelona, Spain. (turiel@icm.csic.es)

E. García-Ladona, Grup d'Oceanografia Física, Institut de Ciències del Mar (CSIC), Passeig Marítim de la Barceloneta 37-49, E-08003 Barcelona, Spain. (emilio@icm.csic.es)

J. Font, Grup d'Oceanografia Física, Institut de Ciències del Mar (CSIC), Passeig Marítim de la Barceloneta 37-49, E-08003 Barcelona, Spain. (jfont@icm.csic.es)

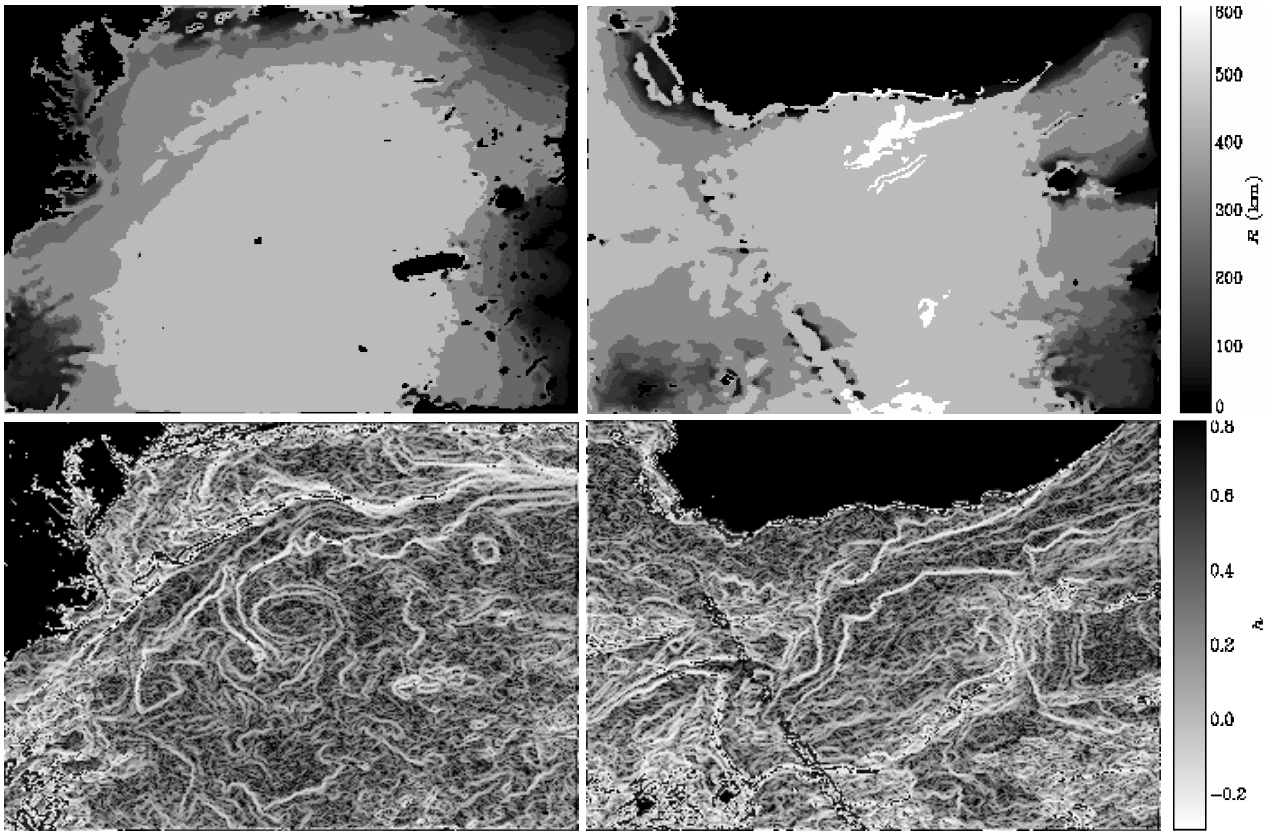

Figure 2. Top: Radius $R(\vec{x})$ for which equation 18 holds for the SST images of figure 1. **Bottom:** Singularity exponents, $h(\vec{x})$, for the same images.

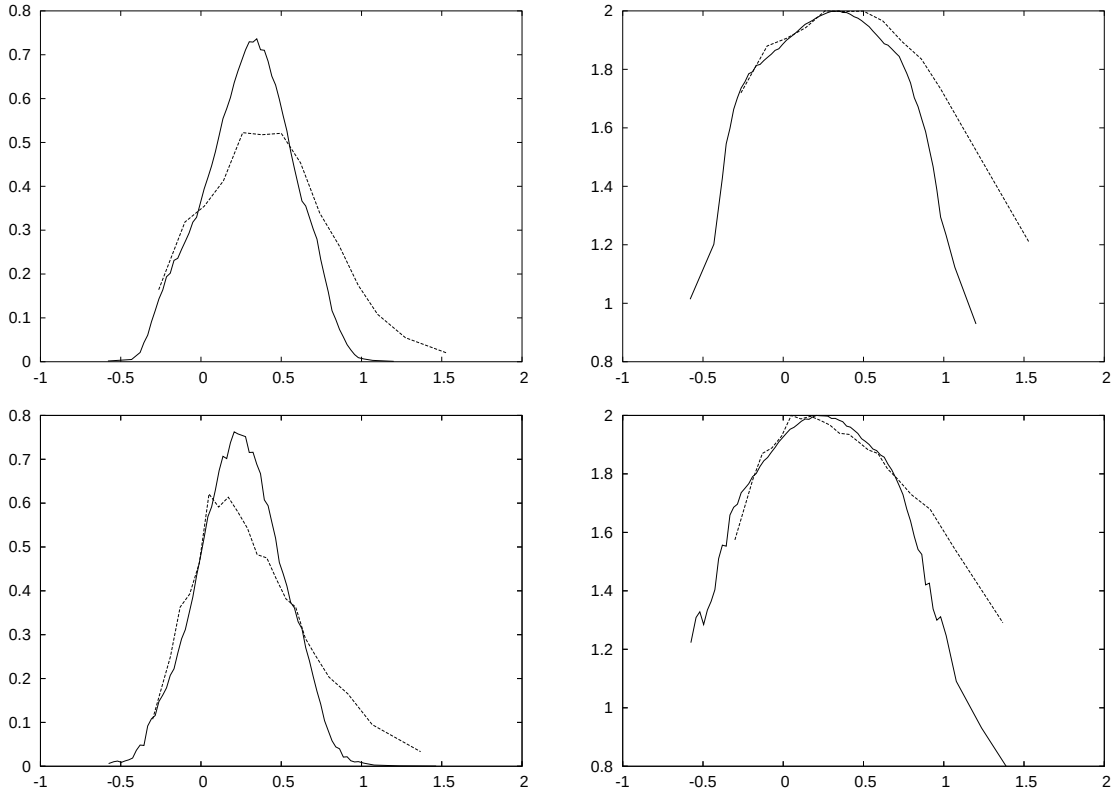

Figure 3. Top left: Empirical PDF's for the singularity exponents over the Gulf Stream area in May 6, 2000. **Top right:** Associated singularity spectra, according to equation (12). **Bottom left:** Empirical PDF's for the singularity exponents over the Agulhas region in November 26, 2002. **Bottom right:** Associated singularity spectra for th Agulhas region. For all graphs, continuous lines correspond to the curves obtained at the minimum possible scale (that of Pathfinder SST image resolution, 4 km) while dashed lines are obtained when the minimum scale is 32 km. Similar results were obtained at different dates and locations.

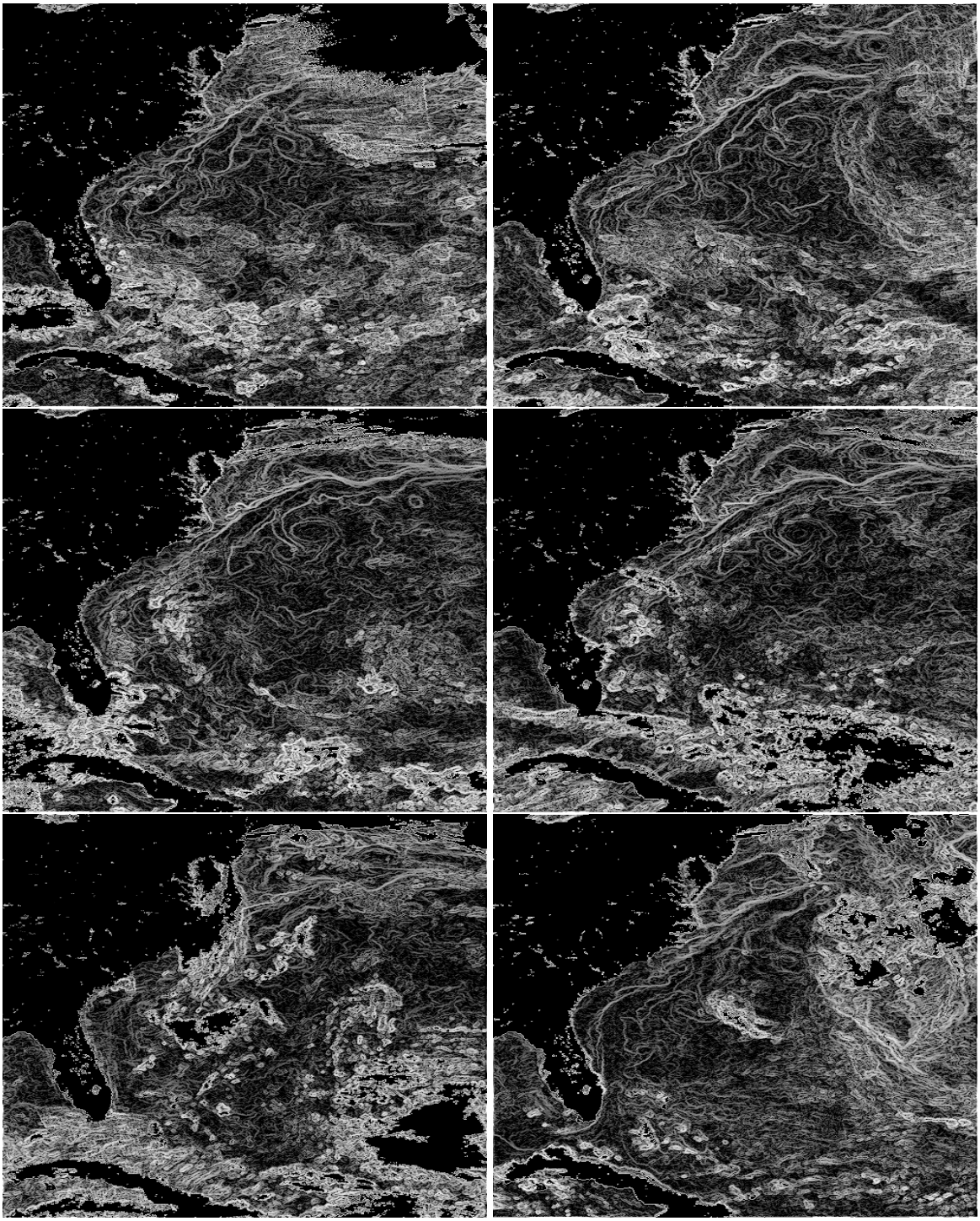

Figure 4. Singularity exponents as obtained from Pathfinder SST images during several days in May, 2000 at the Gulf Stream area. Land pixels and those with temperatures below 5 ^{o} C have been masked to ease comparison. **Top row:** 6 and 7 May. **Middle row:** 8 and 9 May. **Bottom row:** 10 and 13 May.

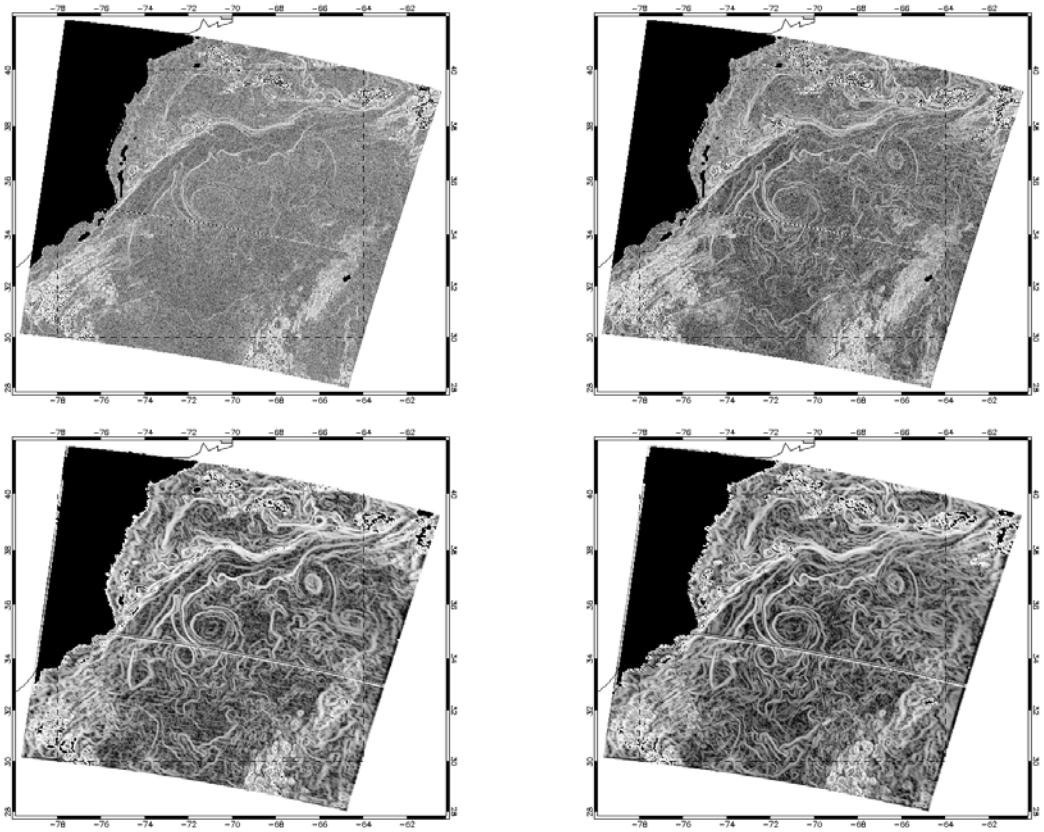

Figure 5. Top: Singularity exponents detected from a SST image (left) and the corresponding channel 31 brightness temperature (right) from MODIS in May 8, 2000 at the Gulf Stream area. **Bottom:** Same results when resolution is reduced by a factor 4 (1 pixel=16 km). The black dashed box corresponds to the area analyzed with Pathfinder SST

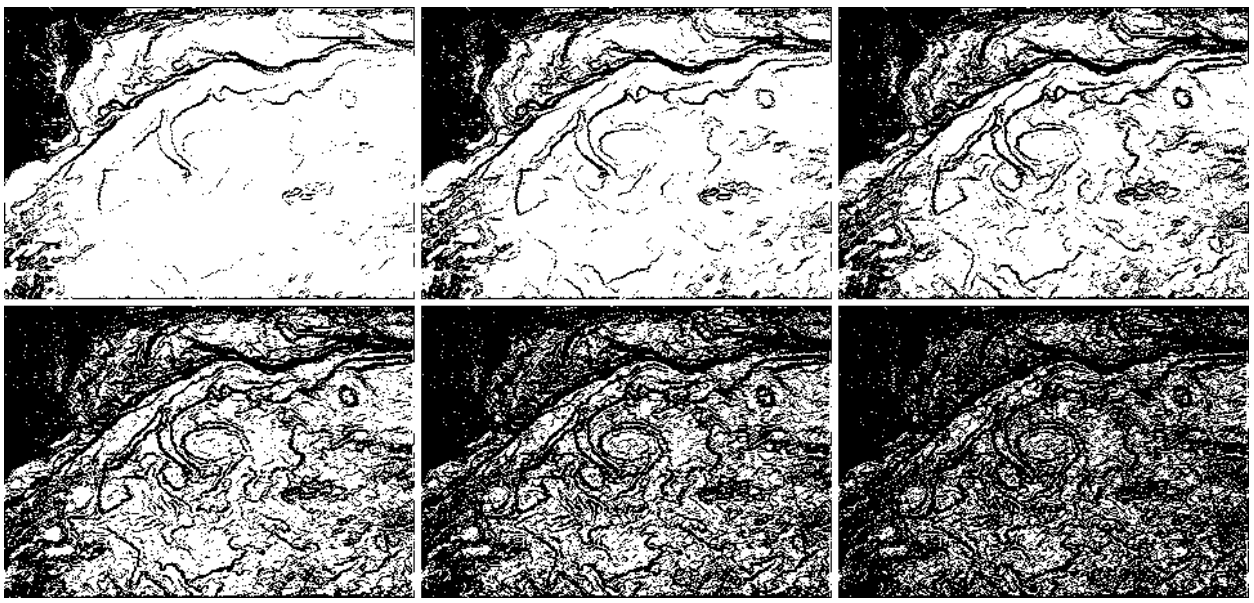

Figure 6. Most Singular Manifold (F_∞) obtained using different values of the threshold exponent (h_0). ¿From left to right and from top to bottom: $h_0 = -0.1$, $h_0 = 0$, $h_0 = 0.1$, $h_0 = 0.2$, $h_0 = 0.3$, $h_0 = 0.4$.

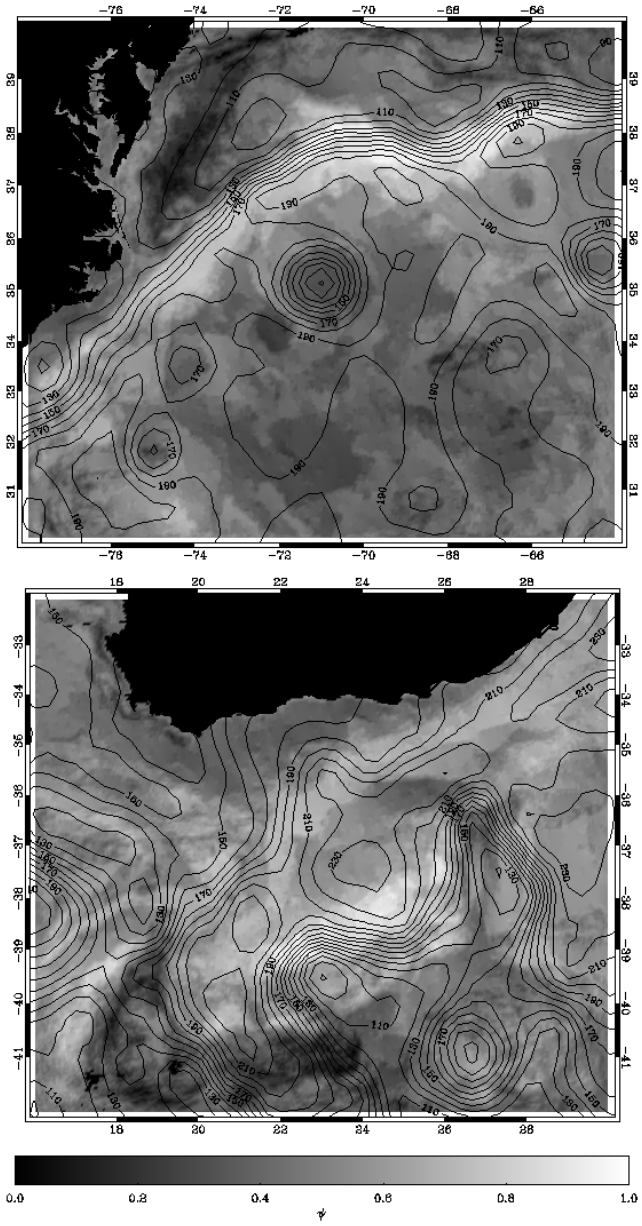

Figure 7. Comparison between the MSS ($\psi_M(\vec{x})$) and the closest sea surface topography map (black lines, units are cm) for the Gulf Stream area (top) and the Agulhas current area (bottom).

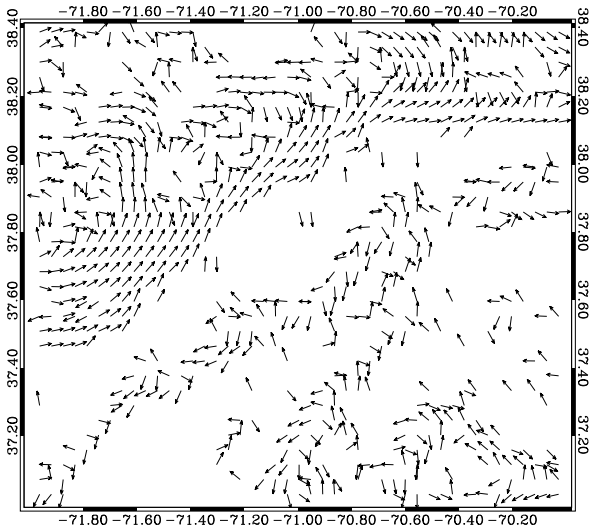

Figure 8. Detail of the non-dimensional velocities on the MSM ($\vec{v}^*_\infty$) for the Gulf Stream current.

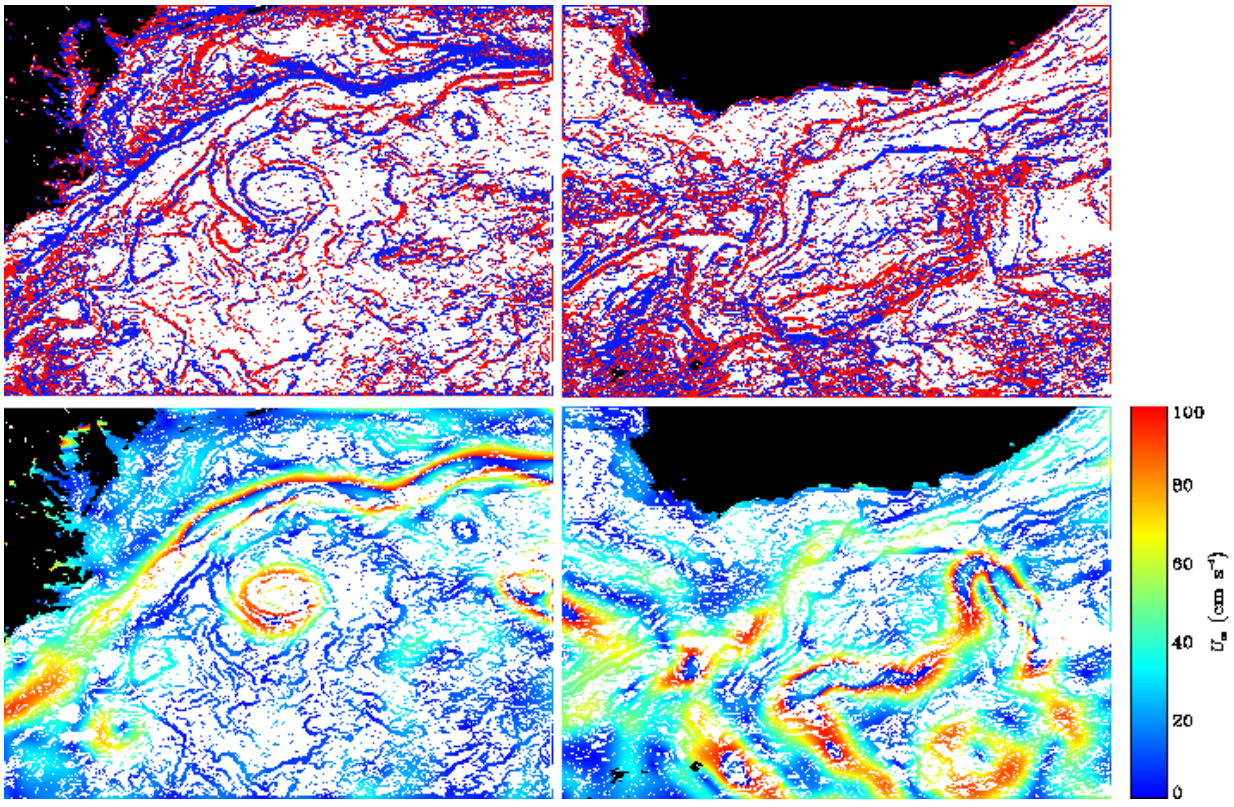

Figure 9. Left column: Gulf Stream images. Right column: Agulhas image. Top figures: MSM with a color code corresponding to the value of U_∞. Bottom figures: MSM with a color code corresponding to ξ_∞

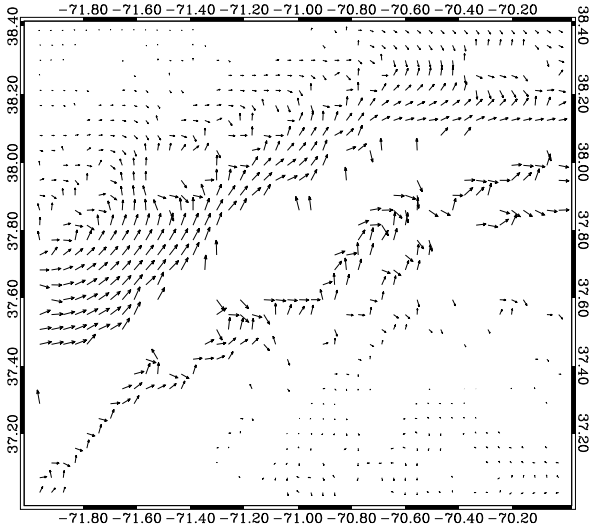

Figure 10. Detail of the calibrated velocities on the MSM ($\vec{v}_{\infty}^{n}$) for the Gulf Stream current.

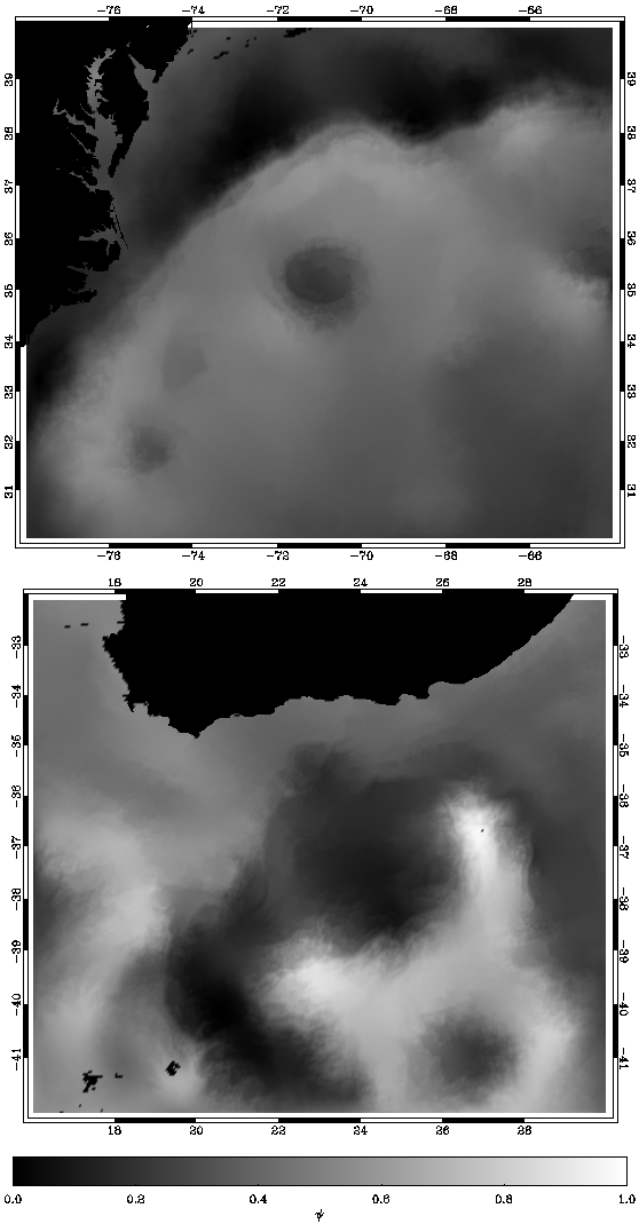

Figure 11. Normalized sreamfunctions ψ_η obtained from the re-calibrated velocities for the Gulf Stream area (top) and the Agulhas current area (bottom).